

# Sulfur Loading and Speciation Control the Hydrophobicity, Electron Transfer, Reactivity, and Selectivity of Sulfidized Nanoscale Zerovalent Iron

Jiang Xu, Astrid Avellan, Hao Li, Xitong Liu, Vincent Noël, Zimo Lou, Yan Wang, Ralf Kaegi, Graeme Henkelman, and Gregory V. Lowry\*

Sulfidized nanoscale zerovalent iron (SNZVI) is a promising material for groundwater remediation. However, the relationships between sulfur content and speciation and the properties of SNZVI materials are unknown, preventing rational design. Here, the effects of sulfur on the crystalline structure, hydrophobicity, sulfur speciation, corrosion potential, and electron transfer resistance are determined. Sulfur incorporation extended the nano-Fe<sup>0</sup> BCC lattice parameter, reduced the Fe local vacancies, and lowered the resistance to electron transfer. Impacts of the main sulfur species (FeS and FeS<sub>2</sub>) on hydrophobicity (water contact angles) are consistent with density functional theory calculations for these FeS<sub>x</sub> phases. These properties well explain the reactivity and selectivity of SNZVI during the reductive dechlorination of trichloroethylene (TCE), a hydrophobic groundwater contaminant. Controlling the amount and speciation of sulfur in the SNZVI made it highly reactive (up to 0.41 L m<sup>-2</sup> d<sup>-1</sup>) and selective for TCE degradation over water (up to 240 moles TCE per mole H<sub>2</sub>O), with an electron efficiency of up to 70%, and these values are 54-fold, 98-fold, and 160-fold higher than for NZVI, respectively. These findings can guide the rational design of robust SNZVI with properties tailored for specific application scenarios.

radionuclides.<sup>[12–17]</sup> However, NZVI is an indiscriminate reductant that also readily reduces water to form hydrogen gas (Fe<sup>0</sup> + 2H<sub>2</sub>O → Fe<sup>2+</sup> + 2OH<sup>-</sup> + H<sub>2(g)</sub>).<sup>[18]</sup> This unwanted side reaction consumes the reducing capacity of the NZVI, decreasing its reactive lifetime, and increases the amount and cost of NZVI required for remediation. Several approaches have been proposed to increase the reactivity or stability of NZVI during remediation, including encapsulating them with polymers or into silica matrices,<sup>[15,19]</sup> doping them with noble metals like Pd or Pt,<sup>[20,21]</sup> and supporting them onto carbon matrices like carbon nanotubes or graphene.<sup>[22,23]</sup> While these approaches improve the injectability of the materials into the subsurface, none have improved the selectivity of NZVI for contaminants over water while still maintaining high reactivity with the target groundwater contaminants. An ideal material for groundwater remediation should possess both high reactivity


and selectivity,<sup>[24]</sup> where the contaminant outcompetes water for reactive sites.

Highly redox active materials are an important tool for the degradation of refractory organic water and soil contaminants.<sup>[1–7]</sup> Nanoscale zero valent (NZVI) has been used for in situ groundwater remediation for more than two decades.<sup>[8–12]</sup> NZVI is a strong reductant that readily dechlorinates chlorinated solvents and antibiotics, and reduces and immobilizes heavy metals and

Recently, it was shown by us and others that the sulfidation of NZVI lowers its reactivity with water and other non-target hydrophilic contaminants (e.g., NO<sub>3</sub><sup>-</sup>), while increasing its reactivity with target contaminants like chlorinated solvents

J. Xu, A. Avellan, X. Liu<sup>[†]</sup>, Z. Lou, G. V. Lowry  
Department of Civil and Environmental Engineering  
Carnegie Mellon University  
Pittsburgh, PA 15213, USA  
E-mail: glowry@cmu.edu

J. Xu, A. Avellan, G. V. Lowry  
Center for Environmental Implications of NanoTechnology  
Carnegie Mellon University  
Pittsburgh, PA 15213, USA

 The ORCID identification number(s) for the author(s) of this article can be found under <https://doi.org/10.1002/adma.201906910>.

<sup>[†]</sup>Present address: Department of Civil and Environmental Engineering, The George Washington University, Washington, D.C. 20052, United States

H. Li, G. Henkelman  
Department of Chemistry and the Oden Institute for Computational Engineering and Sciences  
The University of Texas at Austin  
Austin, Texas 78712, USA

V. Noël  
Stanford Synchrotron Radiation Lightsource  
SLAC National Accelerator Laboratory  
Menlo Park, CA 94025, USA

Y. Wang  
Department of Civil and Environmental Engineering  
University of Pittsburgh  
Pittsburgh, PA 15261, USA

R. Kaegi  
Eawag  
Swiss Federal Institute of Aquatic Science and Technology  
Überlandstrasse 133, 8600 Dübendorf, Switzerland

DOI: 10.1002/adma.201906910

and antibiotics.<sup>[25–31]</sup> Several mechanisms have been hypothesized for the enhanced reactivity and selectivity of sulfidized nanoscale zerovalent iron (SNZVI) compared to NZVI. First, SNZVI is more hydrophobic than NZVI, resulting in lower interaction with water and charged solutes, and greater interaction with hydrophobic contaminants.<sup>[26,29]</sup> Second, the incorporated sulfur lowers electron transfer resistance from Fe<sup>0</sup> to the contaminant.<sup>[32,33]</sup> Third, the incorporated sulfur blocks adsorption sites for atomic hydrogen and inhibits the water reduction reaction and H<sub>2</sub> evolution. All are possible, but evidence for these proposed mechanisms is limited to a few observations, and the limited characterization of SNZVI makes differentiating between these mechanisms difficult.

One common method used to make SNZVI (one-step method) uses dropwise addition of a NaBH<sub>4</sub> and Na<sub>2</sub>S<sub>2</sub>O<sub>4</sub> solution into an aqueous suspension containing dissolved Fe<sup>2+</sup> or Fe<sup>3+</sup> ions. The presence of an FeS (mackinawite) phase either coated onto or mixed with the NZVI particles has been reported, but in many cases without strong experimental evidence to support the claim.<sup>[34–36]</sup> Two recent studies provided experimental evidence for an FeS phase in SNZVI, for example, X-ray absorption spectroscopy analyses<sup>[37]</sup> or X-ray total scattering with pair distribution function analyses.<sup>[38]</sup> Other S species have not been reported. It is widely acquiesced that FeS is the only S species in SNZVI. However, the formation of pyrite is thermodynamically favored under the synthesis conditions, where FeS serves as a precursor for pyrite formation, and reacts with H<sub>2</sub>S to form pyrite.<sup>[39]</sup> It is thus likely that different Fe–sulfur species will form at different amounts of incorporated sulfur. The limited understanding of how S content affects the speciation of S in the structure of the SNZVI and its resulting reactivity and electron transfer efficiency limits the ability to synthesize SNZVI with the best properties for groundwater remediation.

In this work, different amounts of sulfur were incorporated into NZVI particles using a previously described one-step synthesis method.<sup>[40,41]</sup> The physicochemical properties of resulting SNZVI were extensively characterized, including morphology, crystalline structure, sulfur distribution and speciation, hydrophobicity, corrosion tendency, and electron transfer resistance. Differences in these properties explained well the observed reactivity of SNZVI with water and trichloroethylene (TCE). This study advances the understanding of how the properties of SNZVI influence reactivity and selectivity, and paves the way for rational design of SNZVI for different potential application scenarios.

The S/Fe ratio and the Fe<sup>0</sup> content of the particles were determined by measuring total S and Fe by inductively coupled plasma-optical emission spectrometry (ICP-OES) after aqua regia digestion, and by measuring the H<sub>2</sub> formed after acid digestion of the particles (Fe<sup>0</sup> + 2H<sup>+</sup> → Fe<sup>2+</sup> + H<sub>2(g)</sub>), respectively. The S/Fe ratio measured in the particles ([S/Fe]<sub>measured</sub>) increased linearly with the amount of S added during the synthesis ([S/Fe]<sub>dosed</sub>), but [S/Fe]<sub>measured</sub> was always lower than [S/Fe]<sub>dosed</sub> (Figure 1j). The Fe<sup>0</sup> content also decreased linearly with the increased [S/Fe]<sub>measured</sub> (Figure S1, Supporting Information), consistent with the higher amount of S in the particles. The S/Fe molar ratio at the particle surface also increases with increasing [S/Fe]<sub>dosed</sub> according to the X-ray photoelectron spectroscopy (XPS) analysis (Figures S2 and S3, Supporting

Information). The sulfur speciation on the particle surfaces depended on the amount of S in the particles ([S/Fe]<sub>measured</sub>). At all values of [S/Fe]<sub>measured</sub>, sulfides (S<sup>2-</sup>) and disulfides (S<sub>2</sub><sup>2-</sup>) were the dominant species on the surface of the particles. At higher values of [S/Fe]<sub>measured</sub> (>0.082), the S<sub>2</sub><sup>2-</sup> species becomes dominant on the particles' surfaces, along with the formation of polysulfides (S<sub>n</sub><sup>2-</sup>) of up to 18 atom%. The Fe<sup>0</sup> content, [S/Fe]<sub>measured</sub>, and surface sulfur speciation of SNZVI correlate well with the particles' crystalline structure, hydrophobicity, electron transfer resistance, and reactivity with water (H<sub>2</sub> evolution rate) and TCE as described later.

TEM images of NZVI prepared without sulfur shows a chain-like structure of spherical Fe<sup>0</sup> particles that is typical for NZVI made using sodium borohydride reduction (Figure S4, Supporting Information).<sup>[13,42,43]</sup> The addition of sulfur (as sodium dithionite) during the synthesis results in larger particles (Figure 1a–c). The size of the primary particles increased from <100 nm to ≈1 μm when [S/Fe]<sub>measured</sub> was increased from 0 to 0.130. Although larger primary particles were observed with increasing degree of sulfidation, smaller particles of a few 100 nm in diameters were also present in samples sulfidized to the highest degree. Thus, the polydispersity of the particle size distribution also increased with increasing S content. The increase in size was consistent with a decrease in the N<sub>2</sub>-Brunauer–Emmett–Teller specific surface area (Figure S5, Supporting Information). The measured surface area of SNZVI was smaller than those in previous studies,<sup>[40]</sup> which was possibly due to the different preparation procedures (e.g., the concentrations and addition speed of reagents solution) and resulting particle size distribution. XPS analysis of the Fe and O species on the particles' surfaces (Figure S6, Supporting Information) also indicates the presence of oxidized Fe species (e.g., FeOOH and Fe(OH)<sub>2</sub>) and adsorbed OH<sup>-</sup>.<sup>[44,45]</sup> A uniform distribution of sulfur was observed in SNZVI particles with [S/Fe]<sub>measured</sub> = 0.010 (Figure 1d,g; Figure S7a, Supporting Information). At [S/Fe]<sub>measured</sub> = 0.130, the distribution of S was less uniform, and two different particle populations were observed; larger particles with a lower S/Fe ratio, and smaller particles with a higher S/Fe ratio (Figure 1f,i). The similarity of S and Fe distributions of SNZVI with [S/Fe]<sub>measured</sub> = 0.073 (Figure 1e,h) and 0.130 (Line B in Figure 1f,i) indicates that the amount of sulfur that can be incorporated into the NZVI structure is possibly limited. The S was evenly distributed over the particles according to the stable S/Fe ratio in Figure 1g–i, rather than being enriched on the edges as would be expected for a surface coating.<sup>[46]</sup> Excess sulfur in the synthesis method leads to the formation of an S-rich FeS<sub>x</sub> phase rather than more highly sulfidized NZVI particles (Figure 1f,i). The monotonous shift of Fe peaks as increasing S content in the X-ray diffraction (XRD) analysis (Figure 2a) and the improved shell fits by adding Fe–S scattering paths in the X-ray absorption spectroscopy (XAS) analysis (Figure 2b) also suggest the incorporation of S into the Fe BCC structure as discussed later.

The sulfur content affected the water contact angle of SNZVI pellets in air. The contact angle increased sharply with S addition up to a [S/Fe]<sub>measured</sub> = 0.02 to 0.04. Adding more S ([S/Fe]<sub>measured</sub> > 0.07) decreased the water contact angle (Figure 1k; Figure S8, Supporting Information). Although the morphology, sulfur distribution, and/or hydrophobicity of

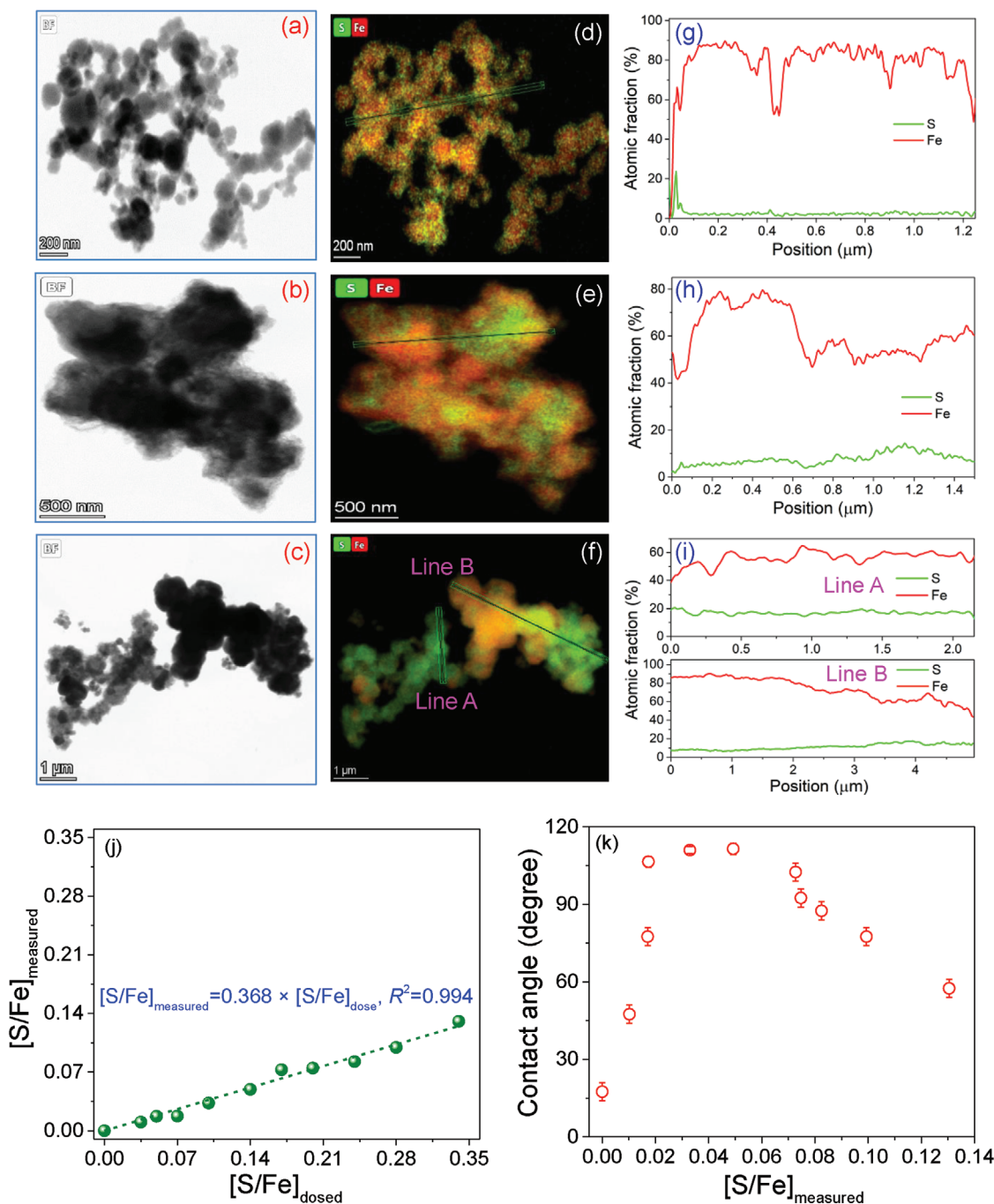


**Figure 1.** Morphology and Fe and S distribution of SNZVI with a, d, g) 0.010, b, e, h) 0.073, and c, f, i) 0.130  $[S/Fe]_{\text{measured}}$  determined by TEM-EDX-mapping analysis; j) actual  $[S/Fe]_{\text{measured}}$  as a function of  $[S/Fe]_{\text{dosed}}$  and k) water contact angle of SNZVI pellets in air as a function of  $[S/Fe]_{\text{measured}}$ .

SNZVI made using a sulfur dose of 0.4 S/Fe molar ratio<sup>[47]</sup> and 0.14 S/Fe molar ratio<sup>[26]</sup> have been reported, the present study indicates that the actual (measured) S content affects the distribution and speciation of S in the structure of SNZVI, the hydrophobicity, and the crystallinity as discussed below.

NZVI made from borohydride reduction of  $Fe^{3+}$  without sulfur incorporation has unique properties compared to larger sized zerovalent iron. For example, this NZVI could dissociate  $H_{2(aq)}$  and use the adsorbed H-atoms for hydrodechlorination

of TCE without a noble metal catalyst.<sup>[43]</sup> This unique reactivity is consistent with the small crystalline scattering domain size observed in XRD patterns (Figure 2a), and the high number of vacancies and a low number of Fe atoms in its body-centered cubic (BCC) structure (Figure 2b) determined by XAS (Table S1, Supporting Information). The XRD results indicate that increasing the S/Fe ratio increased their crystalline X-ray scattering domain size, until reaching a maximum scattering domain size (highest Fe XRD peaks and highest crystallite

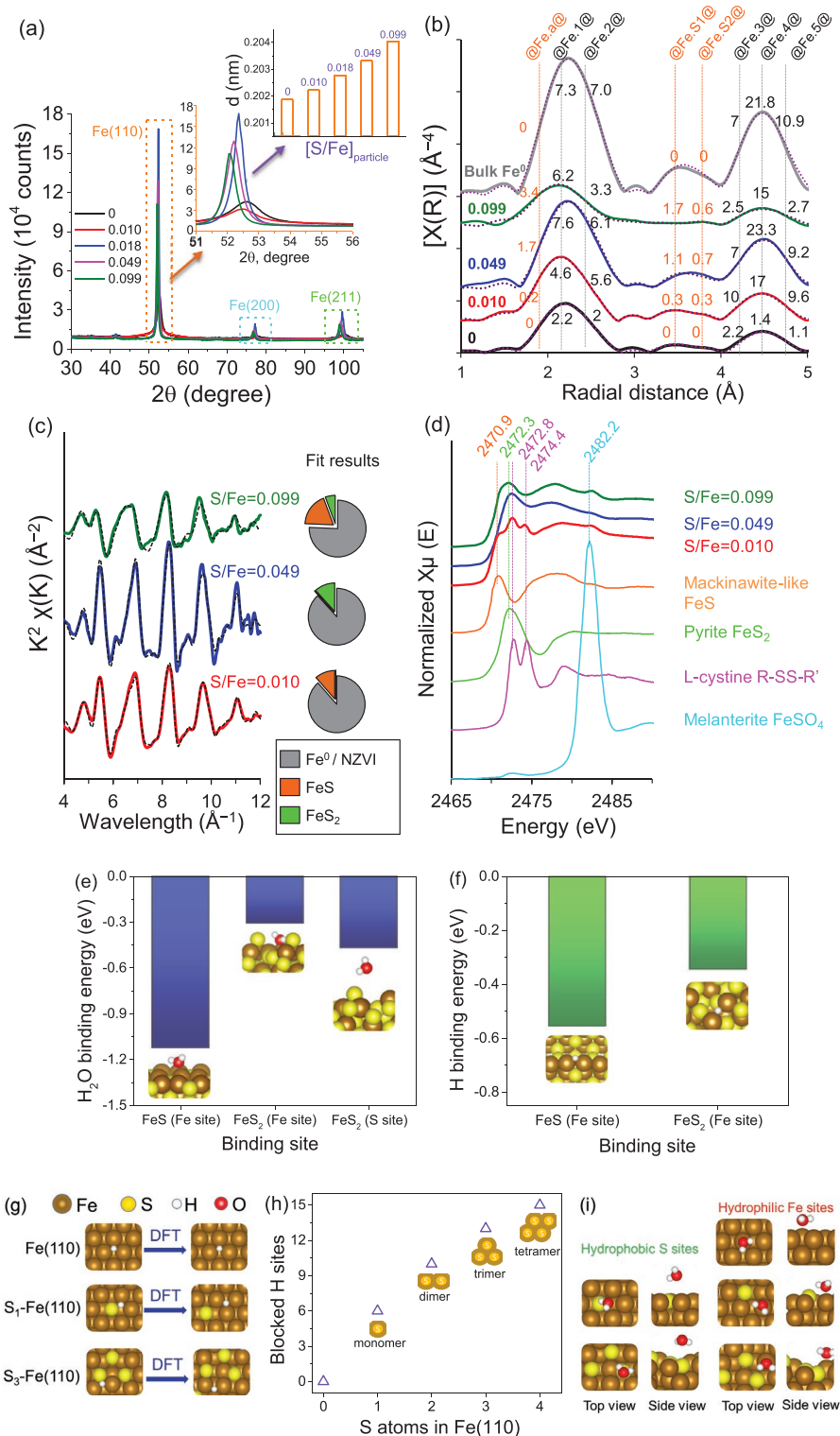


**Figure 2.** Effects of sulfur incorporation on the NZVI crystal structure. a) XRD spectra for the (110), (200), and (211) lattice planes of Fe<sup>0</sup> highlighted in orange, blue and green, respectively. b) Radial structure function of normalized EXAFS spectra (solid lines) and their best shell fits (dotted lines) at the Fe K-edge fitting. Interatomic distances for each scattering path along with the calculated number of coordinated atom (CN) is also reported. See Table S1, Supporting Information, for paths and fitting details. c) Linear combination fits of EXAFS spectra in k<sup>2</sup> space at Fe K-edge. d) XANES spectra along with reference compounds at the S K-edge. e) DFT-calculated adsorption energies of e) water and f) H at the (111) surfaces of mackinawite (FeS) and pyrite (FeS<sub>2</sub>). g) Site evolution of hydrogen adsorption before and after DFT structural relaxations. h) Number of blocked three-fold hollow sites for H adsorption with the increase of surface doped S atoms on Fe(110). i) DFT-optimized adsorption geometries of water at different Fe and S surface ensembles on Fe(110) and S<sub>x</sub>-Fe(110) (x = 1 and 3). Additional information can be found in Table S2, Supporting Information.

size) at  $[S/Fe]_{\text{measured}} = 0.018$  (Figure 2a; Figure S9, Supporting Information). This was consistent for the (110), (200), and (211) planes in the BCC  $Fe^0$  structure. The small peak at  $2\theta = 41^\circ$  is consistent with an Fe(III) oxide ( $Fe_2O_3$ ). The small size of this peak suggests limited oxidation of the Fe had occurred. Other elements (besides Fe, S, and O) were not observed in the XPS survey spectra. This suggests that the materials mainly consisted of Fe, S, and O. Increasing  $[S/Fe]_{\text{measured}}$  also increased the d-spacing in the lattice for all the Fe planes. The monotonic shift of Fe peaks and the linear positive correlation between d-spacing and  $[S/Fe]_{\text{measured}}$  (Figure 2a) suggest that sulfur was incorporated into the BCC Fe crystalline structure forming a solid-solution (alloy compound) rather than forming a phase-segregated structure or a physically mixed structure.<sup>[48,49]</sup>

The  $FeS_x$  phase in SNZVI is often reported or acquiesced to be  $FeS$ .<sup>[34–36]</sup> Here, fitting the Fourier-transformed Fe K-edge extended X-ray absorption fine-structure (EXAFS) spectra with paths corresponding only to the  $Fe^0$  BCC structure resulted in poor fits for all SNZVI samples (Figure S10, Supporting Information). The addition of the paths @Fe.a@, @Fe.S1@, and @Fe.S2@ significantly improved the fits (Figures S10 and S11, Supporting Information), indicating the presence of S within the NZVI structure. The contribution of an Fe–O binding environment in the Fourier-transformed EXAFS spectra was not observed, probably because the amount of Fe–O was below the detection limit. Consistent with the XRD results, shell fitting of the Fe K-edge EXAFS spectra indicates that while all the samples contained a BCC  $Fe^0$  phase, the crystallinity of the structure varies (Figure 2b and Table S1). For  $S/Fe = 0$ , the number of Fe atoms at  $\approx 2.468 \text{ \AA}$  surrounding the absorbing central Fe atom (@Fe.1@ path, see Figure S11 and Table S1, Supporting Information) was significantly lower (coordination number for @Fe.1@<sub>CN</sub> = 2.2) than for a perfect BCC  $Fe^0$  structure (@Fe.1@<sub>CN</sub> = 8) or a bulk  $Fe^0$  structure (@Fe.1@<sub>CN</sub> = 7.3, see Figure 2b; Table S1, Supporting Information), indicating a high number of vacancies in the NZVI structure. Contrary to expectation, adding S into the lattice up to  $S/Fe = 0.049$  decreased the number of vacancies in the  $Fe^0$  BCC crystalline structure (@Fe.1@<sub>CN</sub> values in Figure 2b and Table S1, Supporting Information, increased toward @Fe.1@<sub>CN</sub> = 8 expected for BCC  $Fe^0$ ). The presence of S in the synthesis solution may have slowed the rate of nucleation of  $Fe^0$  or the growth of crystals, resulting in more crystalline structures. However, further increasing the  $S/Fe$  ratio to 0.099 resulted in an SNZVI crystallized structure with lower @Fe.1@<sub>CN</sub>, indicating that a larger amount of S addition eventually disturbs the BCC  $Fe^0$  crystalline structure, consistent with the decrease of maximum peak intensity observed on the XRD spectra and the calculated crystalline scattering domain size (d) (Figure 2a; Figure S9, Supporting Information).

Fitting interatomic distances and coordination number of atomic neighbors at the Fe K-edge was not conclusive about what  $FeS_x$  species formed. Linear combination fitting of the Fe K-edge EXAFS (Figure 2c) suggested primarily  $FeS$  for  $S/Fe = 0.01$ ,  $FeS_2$  for  $S/Fe = 0.049$ , and a mixture of  $FeS + FeS_2$  for  $S/Fe = 0.099$ . This was confirmed with the X-ray absorption near-edge structure (XANES) observations at the S K-edge (Figure 2d) and its derivatives (Figures S12 and S13, Supporting Information). The energy positions correspond to those

expected for mackinawite-like ( $FeS$ ) (2470.9 eV) and pyrite-like ( $FeS_2$ ) (2472.3 eV).<sup>[50,51]</sup> Since  $FeS$  can serve as a precursor for pyrite formation in the presence of  $H_2S$ ,<sup>[39]</sup> it is likely that different S/Fe doses formed different amounts of  $H_2S$  and  $FeS$  in the synthesis, and thus resulted in different amounts of  $FeS$  and  $FeS_2$ . In addition, S K-edge XANES spectra (Figure 2d) indicate the presence of “L-cystine-like” (R-SS-R’) phases in the  $[S/Fe]_{\text{measured}} = 0.01$  sample, and some sulfate precipitation as  $FeSO_{4(s)}$  in all samples. The presence of an L-cystine-like phase (i.e., it matched the spectra of a L-cystine model compound) suggests the presence of a polysulfide phase, which could lower the resistance to electron transfer and improve reactivity because polysulfides (e.g.,  $Fe_3S_4 = 0.0 \text{ eV}$ ) have a lower band gap than other iron sulfides (e.g.,  $FeS = 0.10 \text{ eV}$ ,  $FeS_2 = 0.95 \text{ eV}$ ) or iron oxides (e.g.,  $Fe_2O_3 = 2.2 \text{ eV}$ ).<sup>[52]</sup> This is consistent with the measured electron transfer resistance and reactivity as discussed below. The presence of mackinawite-like and pyrite-like crystal structures likely controls the material’s hydrophobicity because these different  $FeS_x$  phases have different hydrophobicity. However, the poorly ordered  $FeS_x$  phase (observed by TEM-EDX-mapping and measured by XANES at the S K-edge, but not observed in XRD spectra) may also be less hydrophobic than the SNZVI.

The XRD, EXAFS, and XANES results indicate that the S incorporated into the Fe crystalline structure is either organizing as a  $FeS_2$ -like or  $FeS$ -like phase during the synthesis, and that this is dependent on the amount of S added to the system. It should be noted that  $Fe^0$  has a BCC crystal system (Figure S11, Supporting Information), while pyrite ( $FeS_2$ ) has a face-centered cubic (FCC) crystal system, and mackinawite has a tetragonal crystal system. These iron phases have different unit cells, with  $a = 2.86 \text{ \AA}$  for  $Fe^0$ ,  $a = 3.67 \text{ \AA}$  and  $c = 5.20 \text{ \AA}$  for mackinawite, and  $a = 5.40 \text{ \AA}$  for pyrite.<sup>[53,54]</sup> It is not clear how these different crystalline structures organize during the crystal growth of the SNZVI. The addition of  $FeS_x$  structures into the  $Fe^0$  likely apply different “constraints” for the  $Fe^0$  lattice, affecting the d-spacing observed in the XRD results (Figure 2a). Although  $FeS$  was determined to be the main S species in SNZVI either by Fe K-edge XANES or pair distribution function analyses in previous studies,<sup>[37,38]</sup> the complex relationship between the S content and the particle properties has not been captured. In this work, both Fe K-edge EXAFS and S K-edge XANES analysis with appropriate references spectra clearly show how mackinawite ( $FeS$ ) and pyrite ( $FeS_2$ ) species change with S content.

Density functional theory (DFT) calculations were further performed to evaluate the role of sulfur species in the structure and its influence on the affinity to water and H. To compare with our experimental observations, adsorption energies of water and H were calculated on both pyrite ( $FeS_2$ ) and mackinawite ( $FeS$ ). Both the (111) and (001) surfaces are thermodynamically favorable for these materials.<sup>[55–57]</sup> However, due to a significant reconstruction of the (001) surface toward (111) facets upon adsorption (Table S2, Supporting Information), we only analyze the (111) surfaces. As seen in Figure 2e, our DFT calculations show that pyrite adsorbs water more weakly as compared to mackinawite. The DFT-optimized configurations also indicate that pyrite is a more hydrophobic material due to the higher ratio of S on the surface (Table S2, Supporting Information). For all surfaces analyzed, no stable configuration of H

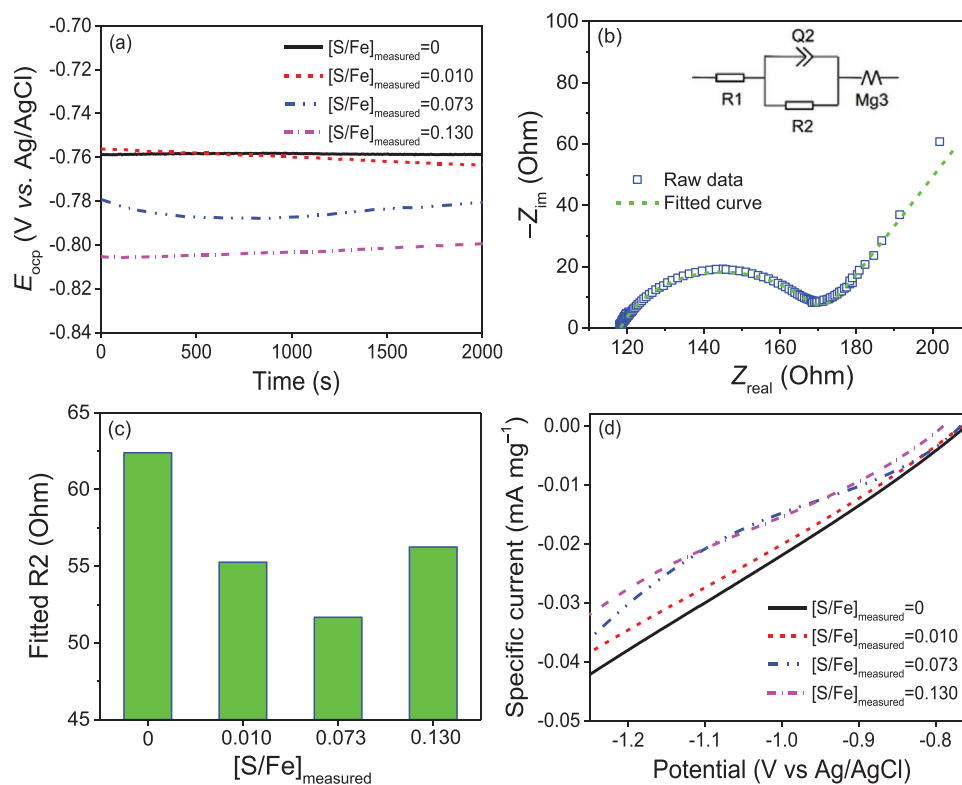


**Figure 3.** Electrochemical characterization of pellets made from NZVI and SNZVI particles; a) open circuit chronopotentiograms; b) Nyquist plot fit to an equivalent circuit model comprised of electrolyte resistance ( $R_1$ ), charge transfer and contact resistance ( $R_2$ ), a constant phase element ( $Q_2$ ), and a Bisquet element ( $Mg_3$ ) ( $[S/Fe]_{\text{measured}} = 0.073$  is shown as an example, others are shown in the SI); c) fitted resistance  $R_2$  for NZVI and three representative SNZVI particles; and d) mass-normalized linear sweep voltammograms at  $2 \text{ mV s}^{-1}$ .

adsorption on S was found; instead, H migrates from the S to Fe site upon optimization (Table S2, Supporting Information). This indicates that the presence of S in SNZVI surfaces significantly hinders H adsorption by reducing the H coverage on the surface. Based upon our calculations, we conclude that the surface with a higher ratio of S (e.g., pyrite) will have a significantly lower affinity to H. The calculated H binding energies at the two materials surfaces also indicate that mackinawite has a significantly stronger H binding energy than pyrite at surface Fe sites (Figure 2f), showing that pyrite is intrinsically more hydrophobic than mackinawite. The presence of these Fe-sulfide materials is expected to make SNZVI more hydrophobic and have fewer H adsorption sites than a pure  $\text{Fe}^0$  surface. To reach a more general conclusion, DFT calculations on the modelled S-doped Fe(110) surfaces were performed to compare with a pure Fe(110) (Figure 2g–i). The presence of S in a Fe structure increases the hydrophobicity of the surface and hinders H adsorption. This unique site-evolution phenomenon can be attributed to the ensemble effect that causes H to migrate from an inert element to a highly active element in an alloyed surface ensemble.<sup>[58]</sup> More importantly, our theoretical studies here demonstrate the hydrophobic nature of sulfur irrespective of how sulfur combines with Fe. Additional information about the computational results and methods can be found in the Supporting Information.

These DFT results correlate well with experimental results that SNZVI with pyrite (e.g.,  $[S/Fe]_{\text{measured}} = 0.049$ )

was more hydrophobic than SNZVI with mackinawite (e.g.,  $[S/Fe]_{\text{measured}} = 0.010$  and  $0.099$ ) and NZVI. The trends in the measured hydrophobicity (Figure 1k) correlated better with the sulfur speciation (Figure 2c), that with sulfur content (Figure 1j). Thus, both sulfur content and speciation determine its properties. It is noteworthy that pyrite has never been reported as species forming during the sulfidation of NZVI in the literature.<sup>[38]</sup> Rather, most studies report  $\text{FeS}$  to be formed from the sulfidation of NZVI.<sup>[34–36]</sup> Our results indicate the presence of pyrite in the SNZVI structure, and SNZVI with pyrite-like structure is more hydrophobic and leads to lower H surface coverage than that with mackinawite. These properties of the pyrite-like structure in SNZVI would also make the material surface more selective for reaction with hydrophobic contaminants over water reduction.

Sulfidation of NZVI has been hypothesized to facilitate electron transfer in previous studies.<sup>[29,30,41,59,60]</sup> However, the impact of sulfur amount and speciation on the electrochemical properties of SNZVI, and on their reactivity and selectivity has not been reported. We prepared electrodes by pressing pellets of NZVI and SNZVI onto Ti mesh and performed several electrochemical tests. The open circuit potential (OCP) was more negative with an increase of  $[S/Fe]_{\text{measured}}$  (Figure 3a), suggesting that sulfur incorporation enhances the tendency of the materials to undergo oxidative corrosion in water. Further, we performed electrochemical impedance spectroscopy (EIS) to probe the charge transfer resistance of SNZVI (Figure 3b,c). EIS

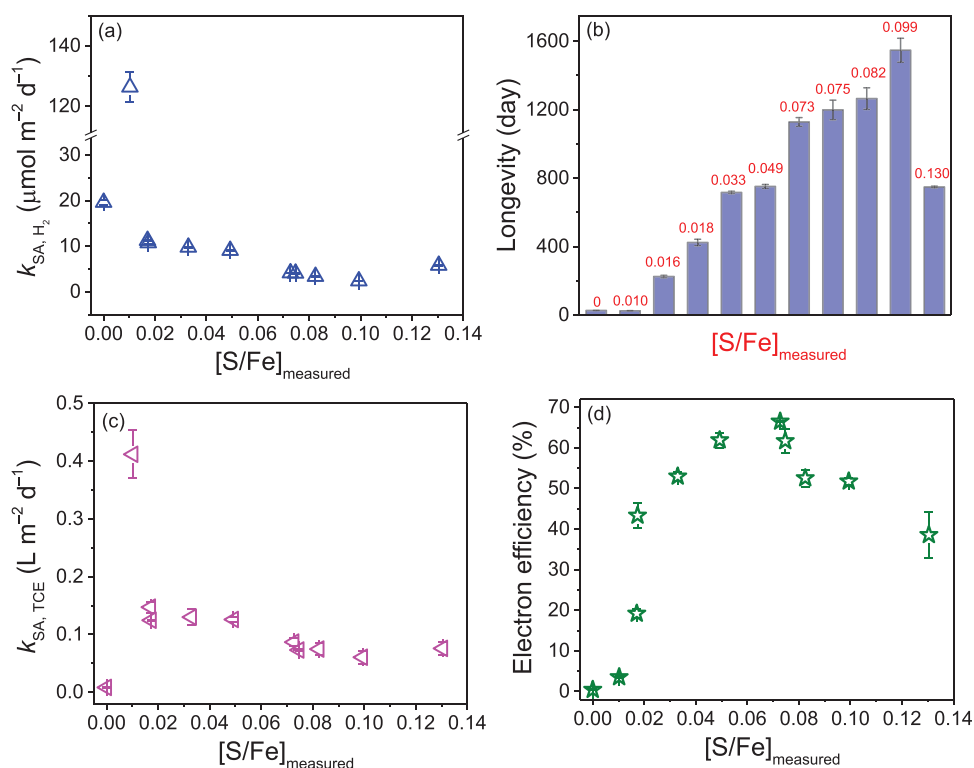


**Figure 4.** Effect of  $[\text{S}/\text{Fe}]_{\text{measured}}$  on a) zero order  $\text{H}_2$  evolution rate ( $k_{\text{SA}, \text{H}_2}$ ) calculated from the 40 days of reaction of  $1.0 \text{ g L}^{-1}$  SNZVI in water. For  $[\text{S}/\text{Fe}]_{\text{measured}} = 0$  and  $0.010$  materials, the  $\text{H}_2$  evolution rates were calculated from the linear (zero order) portion of the curves ( $t < 20 \text{ d}$ ) for comparison with the other materials. b) Estimated reactive lifetime based on the  $\text{Fe}^0$  content and measured  $\text{H}_2$  evolution rates. Effect of  $[\text{S}/\text{Fe}]_{\text{measured}}$  on c)  $k_{\text{SA}, \text{TCE}}$ , and d) electron efficiency TCE degradation using  $1.0 \text{ g L}^{-1}$  SNZVI and an initial TCE concentration of  $90 \mu\text{M}$ .

data were recorded with a 5 mV amplitude sinusoidal potential perturbation over a frequency range of 100 kHz to 10 mHz at the OCP. We fit the Nyquist plots (Figure 3b; Figure S14, Supporting Information) to an equivalent circuit model to derive the resistance  $R_2$ , which includes charge transfer resistance as well as interparticle and particle-mesh contact resistance. Because all samples were pelleted using the same pressure (two tons), SNZVI weight (40 mg), area ( $0.78 \text{ cm}^2$ ), and thickness (0.7 mm), we assume that their contact resistance is the same and observed differences reflect differences in the resistance to electron transfer. The fitted  $R_2$  for SNZVI was lower than that for NZVI (Figure 3c), indicating that sulfidation results in lower charge transfer resistance, that is, it facilitates electron transfer. The specific current in linear sweep voltammograms (LSV) decreased in magnitude with the increase of  $[\text{S}/\text{Fe}]_{\text{measured}}$  (Figure 3d). This result indicates that increasing the sulfur content in the SNZVI particles inhibits  $\text{H}_2$  evolution via the reduction of water. The OCP measures the thermodynamic corrosion tendency, whereas the LSV measures the kinetics of electron transfer. The discrepancy, that is, lower reactivity with water despite a lower resistance to electron transfer suggests that the material's hydrophobicity may be slowing the rate of reaction with water.

The accumulated  $\text{H}_2$  in the headspace of sealed bottles containing SNZVI and water was determined by gas chromatography-thermal conductivity detector (GC-TCD). Compared with NZVI, the lowest amount of sulfur ( $[\text{S}/\text{Fe}]_{\text{measured}} = 0.010$ ) significantly increased the surface-area-normalized rate

of  $\text{H}_2$  evolution ( $k_{\text{SA}, \text{H}_2}$ ) by SNZVI (Figure 4a). This is likely because the electron transfer resistance was significantly lowered (Figure 3c), but the material remained hydrophilic (water contact angle =  $45^\circ$ ) and the small amount of S blocked a limited number of H adsorption sites. Further increasing sulfur content in SNZVI gradually increased its hydrophobicity and decreased the reaction between SNZVI and water. Although the SNZVI was less hydrophobic when  $[\text{S}/\text{Fe}]_{\text{measured}} > 0.049$ , the  $\text{H}_2$  evolution by SNZVI continued to decrease because more H sites were blocked by the increased sulfur in SNZVI as shown in DFT results (Figure 2h). The properties endowed by sulfidation (hydrophobicity, blocking H adsorption sites, and improving electron transfer) clearly make the SNZVI less reactive with water, but may increase the reactivity with TCE as discussed below.

The reactive lifetime of SNZVI (i.e., the time when all of the  $\text{Fe}^0$  is depleted) in deionized water was estimated by dividing its initial  $\text{Fe}^0$  content (Figure S1, Supporting Information) by its  $\text{H}_2$  evolution rate ( $\% \text{ d}^{-1}$ ) determined over 40 days (Figure S15, Supporting Information). Note that this reactive lifetime estimation was determined in deionized water in the absence of other competing oxidants (e.g., TCE, nitrate, dissolved oxygen) that would also affect reactive lifetime, and other ions that do not necessarily take part in redox reactions but could affect the  $\text{Fe}^0$  corrosion rate (e.g.,  $\text{Cl}^-$ ,  $\text{HCO}_3^-$ , and  $\text{SO}_4^{2-}$ ).<sup>[61–63]</sup> Regardless, there is a remarkable advantage of the sulfidized materials over the unsulfidized materials with respect to its corrosion rate by water, and the impact depends on the  $[\text{S}/\text{Fe}]_{\text{measured}}$

in the particles. The estimated lifetime of SNZVI with  $[S/Fe]_{\text{measured}} = 0.099$  was the highest, up to  $\approx 4.2$  years, which was 58-fold higher than that of NZVI. Note that neither the most hydrophobic material nor the highest  $[S/Fe]_{\text{measured}}$  material showed the highest longevity. This is because the optimum occurs at an intermediate amount of incorporated S that maximizes  $Fe^{\circ}$  content and minimizes reactivity with water.

NZVI has high reactivity with water to form hydrogen and low reactivity with TCE (Figure 4a). This leads to poor selectivity and inefficient use of the NZVI. Increasing the S content in SNZVI indeed increases the reactivity with TCE (Figure 4c; Figure S16, Supporting Information). The S content and speciation, DFT calculations, hydrophobicity, and electron transfer resistance of different materials could fully explain their reactivity with water and TCE. For instance, the surface-area-normalized rate constant of TCE removal ( $k_{SA, TCE}$ ) by 0.010  $[S/Fe]_{\text{measured}}$  material was highest in this study, which was  $\approx 50$ -fold and  $\approx$ fourfold higher than that of unmodified NZVI and other SNZVI, respectively. The electron transfer resistance was much lower than unmodified NZVI (Figure 3c), which may explain its higher reactivity. However, this material was also highly reactive with water, likely due to its higher hydrophilicity (Figure 1k) and limited S content, resulting in more H adsorption sites than those with higher S content (Figure 2h). As a result, the selectivity of this material for TCE was low (Figure 4d). The  $[S/Fe]_{\text{measured}} = 0.049$  material containing only pyrite was more hydrophobic and selective for TCE reduction than the  $[S/Fe]_{\text{measured}} = 0.010$  and  $[S/Fe]_{\text{measured}} = 0.099$  materials, that is, higher ratio of reaction rate with TCE relative to water ( $k_{SA, TCE}/k_{SA, H_2}$ ). The more hydrophilic  $[S/Fe]_{\text{measured}} = 0.099$  material (water contact angle  $\approx 80^{\circ}$ ) had a lower selectivity ( $k_{SA, TCE}/k_{SA, H_2}$ ), despite also having a lower reactivity with water. This is due to its lower reaction rate with TCE (less hydrophobic) and its lower reactivity with water (higher S content). However, the lower reactivity of  $[S/Fe]_{\text{measured}} = 0.099$  with water led to a longer predicted reactive lifetime in water (Figure 4b) because this prediction only considers reactivity with water. Indeed, the hydrophobicity appears to be an important factor for electron selectivity, but the S/Fe ratio also plays a role in the overall electron efficiency (Figure S17, Supporting Information). The electron efficiency of TCE removal by SNZVI was as high as 70%, which was  $\approx 160$ -fold higher than that by NZVI ( $< 0.5\%$ ). The high selectivity and low reactivity with water indicates that SNZVI will perform better as an in situ remediation material compared to NZVI.

In summary, SNZVI particles with different physicochemical properties were successfully synthesized via tuning the incorporated amount of sulfur into the Fe crystalline structure. The properties controlling SNZVI reactivity include the sulfur amount, distribution and speciation, hydrophobicity, and crystalline structure. Sulfur incorporation into NZVI indeed makes it more hydrophobic, blocks H adsorption sites, and reduces the electron transfer resistance compared to NZVI. This makes SNZVI more reactive with TCE but less reactive with water. SNZVI containing a higher fraction of pyrite is more hydrophobic and selective for TCE over water than SNZVI containing mackinawite. These fundamental findings will guide the rational design of SNZVI with controllable properties for environmental remediation.

## Experimental Section

**Synthesis of SNZVI:** Briefly, SNZVI was synthesized by dropwise addition ( $\approx 7 \text{ mL min}^{-1}$ ) of 200 mL of a  $34 \text{ g L}^{-1}$   $NaBH_4$  (98%, Fisher Scientific) and  $1.6 \text{ g L}^{-1}$   $Na_2S_2O_4$  ( $\geq 88\%$ , Sinopharm Chemical Reagent Co., Ltd., China) solution into 200 mL of a  $29 \text{ g L}^{-1}$   $FeCl_3$  (97%, Sigma-Aldrich) solution while stirring at 600 rpm under nitrogen.<sup>[26]</sup> This theoretically provides a  $[S/Fe]_{\text{dosed}}$  ratio of 0.10. SNZVI particles with different  $[S/Fe]_{\text{dosed}}$  ratios (0, 0.035, 0.05, 0.07, 0.10, 0.14, 0.17, 0.20, 0.24, 0.28, and 0.34) were synthesized using the same procedure, except changing the concentration of  $Na_2S_2O_4$ . All of the as-prepared SNZVI suspensions were washed three times with deoxygenated deionized water and recovered using magnetic separation. After decanting the liquid, the particles were dried in a vacuum oven at  $60^{\circ}\text{C}$  for 8 hours. The vacuum was slowly filled by air over 3 hours to let the material partially oxidize and stabilize before moving them into an anaerobic glovebox. The dry particles were then ground in a mortar using a pestle and stored in sealed vials in the anaerobic glovebox. Detailed measurements of  $Fe^{\circ}$  content and S/Fe molar ratio in the particles are described in the Supporting Information.

**Batch Experiments:** Batch studies of NZVI or SNZVI reactivity with water and TCE were conducted in 160 mL serum bottles containing 60 mL of headspace and 100 mL of deoxygenated DI water (pH  $\approx 6.0$ ) with or without  $90 \mu\text{M}$  TCE, respectively. Bottles were rotated on an end-over-end rotator at 30 rpm at  $22 \pm 2^{\circ}\text{C}$  after capped by Teflon Mininert valves. The reactions of NZVI or SNZVI with water and TCE were monitored over 60 days and 8 days, respectively. Detailed measurements of  $H_2$ , TCE, and main products are described in the Supporting Information.

**Characterizations of NZVI and SNZVI:** The morphology and elemental distributions of individual particles were assessed using a transmission electron microscopy (TEM, Talos, FEI, 200 kV) connected to an energy dispersive X-ray (EDX) system (Super-X EDS, four detector configurations, FEI). X-ray diffraction (XRD, Rigaku Geigerflex with  $Co K\alpha$  X-ray source), X-ray Photoelectron Spectroscopy (XPS, ESCALAB 250Xi) with an Al  $K\alpha$  monochromatic X-ray source (1486.7 eV, spot size  $650 \mu\text{m}$ ), and Brunauer–Emmett–Teller (BET, Quantachrome 02108-KR-1) were used to obtain the crystallinity, sulfur species on the surface, and the specific surface area of the particles, respectively. Note that a cobalt X-ray source was used for XRD analysis because it is more sensitive to Fe phases than the commonly used copper source. This shifts all energies of diffraction peaks (e.g.,  $Fe(110)$  from  $2\theta = 44.9^{\circ}$  to  $52.5^{\circ}$  for NZVI) but makes phase identification unambiguous.<sup>[64]</sup> The structure of SNZVI with different  $[S/Fe]$  ratio was studied using feature recognition of X-ray Near Edge Structure (XANES) features at the S K-edge, linear combination fitting of the Extended X-Ray Absorption Fine Structure (EXAFS) at the Fe K-edge, or shell fitting of its Fourier transformed spectra. Detailed methods of EXAFS and XANES analysis are described in the Supporting Information.

**Water Contact Angle Measurement:** Three 7 mm (diameter) by 1 mm (thick) pellets of each material were prepared using a Quickpress (PerkinElmer), which were dried in a vacuum oven at  $60^{\circ}\text{C}$  for 8 h, followed by gradually releasing the pressure with air over 1 h. The vacuum-dried pellets were briefly exposed to air before measuring the contact angle using a goniometer (Rame-Hart). Air exposure could affect the  $FeS_x$  composition. However, the water contact angle of each pellet was stable during the measurements. Moreover, there were significant differences in the measured water contact angle, suggesting that exposure to air did not transform the particles significantly.

**Electrochemical Tests:** Open circuit potential (OCP) measurements, electrochemical impedance spectroscopy (EIS), and linear sweep voltammetry (LSV) analysis of NZVI and SNZVI electrodes are performed to study their electrochemical properties. Detailed procedure is described in the Supporting Information.

**DFT Calculations:** The DFT were performed to study the water and H adsorption on the thermodynamically favorable (111) and (001) surfaces of the mackinawite and pyrite, and on the main  $Fe(110)$  surfaces with or without sulfur incorporation of Fe structure, obtaining the role of



sulfur in the hydrophobicity and blocking H adsorption sites of SNZVI surfaces. Detailed methods are described in the Supporting Information.

## Supporting Information

Supporting Information is available from the Wiley Online Library or from the author.

## Acknowledgements

The authors thank the NSF and EPA funding under NSF Cooperative Agreement EF-1266252, Center for the Environmental Implications of NanoTechnology (CEINT) for partial support. Portions of this research were carried out at the SSRL beamline 4-3, 4-1 and 11-2, a national user facility operated by Stanford University on behalf of the U.S. Department of Energy, Office of Basic Energy Sciences. The authors thank Ryan Davis at SSRL (BL 4-1) and (11-2), Matthew Latimer and Erik Nelson (BL 4-3) for their support. SSRL is supported by the U.S. Department of Energy, Office of Science, Office of Basic Energy Sciences under Contract No. DE-AC02-76SF00515, the DOE Office of Biological and Environmental Research, and the National Institutes of Health, National Institute of General Medical Sciences (including P41GM103393). The calculations were supported by the Welch Foundation (F-1841) and the Texas Advanced Computing Center.

## Conflict of Interest

The authors declare no conflict of interest.

## Keywords

environmental nanotechnology, groundwater remediation, rational design, sulfidized nanoscale zerovalent iron, sulfur speciation

Received: October 21, 2019

Revised: January 27, 2020

Published online:

- [1] R. Feng, W. Lei, G. Liu, M. Liu, *Adv. Mater.* **2018**, *30*, 1804770.
- [2] J. Cai, J. Huang, S. Wang, J. Iocozzia, Z. Sun, J. Sun, Y. Yang, Y. Lai, Z. Lin, *Adv. Mater.* **2019**, *31*, 1806314.
- [3] E. T. Martin, C. M. McGuire, M. S. Mubarak, D. G. Peters, *Chem. Rev.* **2016**, *116*, 15198.
- [4] C. Hu, Y. Lin, J. W. Connell, H. Cheng, Y. Gogotsi, M. Titirici, L. Dai, *Adv. Mater.* **2019**, *31*, 1806128.
- [5] H. Li, S. Gan, H. Wang, D. Han, L. Niu, *Adv. Mater.* **2015**, *27*, 6906.
- [6] P. Shao, J. Tian, F. Yang, X. Duan, S. Gao, W. Shi, X. Luo, F. Cui, S. Luo, S. Wang, *Adv. Funct. Mater.* **2018**, *28*, 1705295.
- [7] G. Zhang, Q. Ji, Z. Wu, G. Wang, H. Liu, J. Qu, J. Li, *Adv. Funct. Mater.* **2018**, *28*, 1706462.
- [8] C. Wang, W. Zhang, *Environ. Sci. Technol.* **1997**, *31*, 2154.
- [9] N. C. Mueller, J. Braun, J. Bruns, M. Černík, P. Rissing, D. Rickerby, B. Nowack, *Environ. Sci. Pollut. R.* **2012**, *19*, 550.
- [10] S. M. Ponder, J. G. Darab, T. E. Mallouk, *Environ. Sci. Technol.* **2000**, *34*, 2564.
- [11] S. J. Tesh, T. B. Scott, *Adv. Mater.* **2014**, *26*, 6056.
- [12] J. Xu, X. Liu, G. V. Lowry, Z. Cao, H. Zhao, J. L. Zhou, X. Xu, *ACS Appl. Mater. Interfaces* **2016**, *8*, 7333.
- [13] Y. Liu, S. A. Majetich, R. D. Tilton, D. S. Sholl, G. V. Lowry, *Environ. Sci. Technol.* **2005**, *39*, 1338.
- [14] X. Liu, Z. Cao, Z. Yuan, J. Zhang, X. Guo, Y. Yang, F. He, Y. Zhao, J. Xu, *Chem. Eng. J.* **2018**, *334*, 508.
- [15] Y. Zou, X. Wang, A. Khan, P. Wang, Y. Liu, A. Alsaedi, T. Hayat, X. Wang, *Environ. Sci. Technol.* **2016**, *50*, 7290.
- [16] L. Ling, X. Huang, W. Zhang, *Adv. Mater.* **2018**, *30*, 1705703.
- [17] L. Ling, W. Zhang, *J. Am. Chem. Soc.* **2015**, *137*, 2788.
- [18] Y. Liu, G. V. Lowry, *Environ. Sci. Technol.* **2006**, *40*, 6085.
- [19] S. Luo, T. Lu, L. Peng, J. Shao, Q. Zeng, J. Gu, *J. Mater. Chem. A* **2014**, *2*, 15463.
- [20] J. Xu, J. Tang, S. A. Baig, X. Lv, X. Xu, *J. Hazard. Mater.* **2013**, *244–245*, 628.
- [21] W. Zhang, C. Wang, H. Lien, *Catal. Today* **1998**, *40*, 387.
- [22] J. Xu, T. Sheng, Y. Hu, S. A. Baig, X. Lv, X. Xu, *Chem. Eng. J.* **2013**, *219*, 162.
- [23] Y. Sun, C. Ding, W. Cheng, X. Wang, *J. Hazard. Mater.* **2014**, *280*, 399.
- [24] T. Zhang, G. V. Lowry, N. L. Capiro, J. Chen, W. Chen, Y. Chen, D. D. Dionysiou, D. W. Elliott, S. Ghoshal, T. Hofmann, H. Hsu-Kim, J. Hughes, C. Jiang, G. Jiang, C. Jing, M. Kavanaugh, Q. Li, S. Liu, J. Ma, B. Pan, T. Phenrat, X. Qu, X. Quan, N. Saleh, P. J. Vikesland, Q. Wang, P. Westerhoff, M. S. Wong, T. Xia, B. Xing, B. Yan, L. Zhang, D. Zhou, P. J. J. Alvarez, *Environ. Sci. Nano* **2019**, *6*, 1283.
- [25] Z. Cao, X. Liu, J. Xu, J. Zhang, Y. Yang, J. Zhou, X. Xu, G. V. Lowry, *Environ. Sci. Technol.* **2017**, *51*, 11269.
- [26] J. Xu, Y. Wang, C. Weng, W. Bai, Y. Jiao, R. Kaegi, G. V. Lowry, *Environ. Sci. Technol.* **2019**, *53*, 5936.
- [27] D. Fan, G. O'Brien Johnson, P. G. Tratnyek, R. L. Johnson, *Environ. Sci. Technol.* **2016**, *50*, 9558.
- [28] S. Bhattacharjee, S. Ghoshal, *Environ. Sci. Technol.* **2018**, *52*, 11078.
- [29] F. He, Z. Li, S. Shi, W. Xu, H. Sheng, Y. Gu, Y. Jiang, B. Xi, *Environ. Sci. Technol.* **2018**, *52*, 8627.
- [30] J. Xu, Z. Cao, Y. Wang, Y. Zhang, X. Gao, M. B. Ahmed, J. Zhang, Y. Yang, J. L. Zhou, G. V. Lowry, *Chem. Eng. J.* **2019**, *359*, 713.
- [31] J. Xu, Z. Cao, H. Zhou, Z. Lou, Y. Wang, X. Xu, G. V. Lowry, *Environ. Sci. Technol.* **2019**, *53*, 13344.
- [32] J. Li, X. Zhang, M. Liu, B. Pan, W. Zhang, Z. Shi, X. Guan, *Environ. Sci. Technol.* **2018**, *52*, 2988.
- [33] D. Fan, Y. Lan, P. G. Tratnyek, R. L. Johnson, J. Filip, D. M. O'Carroll, A. Nunez Garcia, A. Agrawal, *Environ. Sci. Technol.* **2017**, *51*, 13070.
- [34] E. Kim, K. Murugesan, J. Kim, P. G. Tratnyek, Y. Chang, *Ind. Eng. Chem. Res.* **2013**, *52*, 9343.
- [35] Q. Zhang, W. Guo, X. Yue, Z. Liu, X. Li, *Environ. Prog. Sustain.* **2016**, *35*, 1673.
- [36] D. Turcio-Ortega, D. Fan, P. G. Tratnyek, E. Kim, Y. Chang, *Environ. Sci. Technol.* **2012**, *46*, 12484.
- [37] S. Song, Y. Su, A. S. Adeleye, Y. Zhang, X. Zhou, *Appl. Catal. B Environ.* **2017**, *201*, 211.
- [38] M. Mangayayam, K. Dideriksen, M. Ceccato, D. J. Tobler, *Environ. Sci. Technol.* **2019**, *53*, 4389.
- [39] D. Rickard, G. W. Luther, *Chem. Rev.* **2007**, *107*, 514.
- [40] E. Kim, J. Kim, A. Azad, Y. Chang, *ACS Appl. Mater. Interfaces* **2011**, *3*, 1457.
- [41] D. Lv, J. Zhou, Z. Cao, J. Xu, Y. Liu, Y. Li, K. Yang, Z. Lou, L. Lou, X. Xu, *Chemosphere* **2019**, *224*, 306.
- [42] Y. Sun, X. Li, J. Cao, W. Zhang, H. P. Wang, *Adv. Colloid Interf.* **2006**, *120*, 47.
- [43] Y. Liu, H. Choi, D. Dionysiou, G. V. Lowry, *Chem. Mater.* **2005**, *17*, 5315.
- [44] A. P. Grosvenor, B. A. Kobe, N. S. McIntyre, *Surf. Sci.* **2004**, *572*, 217.
- [45] G. Bhargava, I. Gouzman, C. M. Chun, T. A. Ramanarayanan, S. L. Bernasek, *Appl. Surf. Sci.* **2007**, *253*, 4322.
- [46] E. Spielman-Sun, E. Lombi, E. Donner, A. Avellan, B. Etschmann, D. Howard, G. V. Lowry, *Environ. Sci. Technol.* **2018**, *52*, 9777.

- [47] Y. Su, D. Jassby, S. Song, X. Zhou, H. Zhao, J. Filip, E. Petala, Y. Zhang, *Environ. Sci. Technol.* **2018**, *52*, 6466.
- [48] N. W. Ashcroft, A. R. Denton, *Phys. Rev. A* **1991**, *43*, 3161.
- [49] H. Guo, H. Li, K. Jarvis, H. Wan, P. Kunal, S. G. Dunning, Y. Liu, G. Henkelman, S. M. Humphrey, *ACS Catal.* **2018**, *8*, 11386.
- [50] M. Ikogou, G. Ona-Nguema, F. Juillot, P. Le Pape, N. Menguy, N. Richeux, J. Guigner, V. Noël, J. Brest, B. Baptiste, G. Morin, *Appl. Geochem.* **2017**, *80*, 143.
- [51] V. Noël, K. Boye, R. K. Kukkadapu, S. Bone, J. S. Lezama Pacheco, E. Cardarelli, N. Janot, S. Fendorf, K. H. Williams, J. R. Bargar, *Sci. Total Environ.* **2017**, *603–604*, 663.
- [52] Y. Xu, M. A. A. Schoonen, *Am. Mineral.* **2000**, *85*, 543.
- [53] R. A. B. K. John, (Ed: W. Anthony), *Handbook of Mineralogy*, Mineralogical Society of America, Chantilly, VA, USA. <http://www.handbookofmineralogy.org/>, **1990**.
- [54] H. Y. Jeong, J. H. Lee, K. F. Hayes, *Geochim. Cosmochim. Ac.* **2008**, *72*, 493.
- [55] M. Blanchard, K. Wright, J. D. Gale, C. R. A. Catlow, *J. Phys. Chem. C* **2007**, *111*, 11390.
- [56] N. Y. Dzade, A. Roldan, N. H. de Leeuw, *J. Chem. Phys.* **2015**, *143*, 94703.
- [57] A. Hung, J. Muscat, I. Yarovsky, S. P. Russo, *Surf. Sci.* **2002**, *520*, 111.
- [58] H. Li, K. Shin, G. Henkelman, *J. Chem. Phys.* **2018**, *149*, 174705.
- [59] Y. Han, W. Yan, *Environ. Sci. Technol.* **2016**, *50*, 12992.
- [60] J. Li, X. Zhang, Y. Sun, L. Liang, B. Pan, W. Zhang, X. Guan, *Environ. Sci. Technol.* **2017**, *51*, 13533.
- [61] E. J. Reardon, *Environ. Sci. Technol.* **1995**, *29*, 2936.
- [62] C. Le, J. H. Wu, S. B. Deng, P. Li, X. D. Wang, N. W. Zhu, P. X. Wu, *Water Sci. Technol.* **2011**, *63*, 1485.
- [63] J. Xu, L. Tan, S. A. Baig, D. Wu, X. Lv, X. Xu, *Chem. Eng. J.* **2013**, *231*, 26.
- [64] Y. M. Mos, A. C. Vermeulen, C. J. N. Buisman, J. Weijma, *Geomicrobiol. J.* **2018**, *35*, 511.